

# Self-aggregation determined by cold pool collisions

Silas Boye Nissen\* and Jan O. Haerter†

*Niels Bohr Institute  
University of Copenhagen  
Blegdamsvej 17, 2100 Copenhagen  
Denmark*

(Dated: September 8, 2022)

In radiative-convective equilibrium (RCE) simulations, the initial pattern of convective cells is often considered to be unorganized, or random [1]. Eventually, symmetry breaking, known as self-aggregation, occurs [2]. We show that the pattern of cells is already non-random a few hours after the initial onset of convection, and that cloud patterns organize into line-like structures. We suggest that the formation of these lines requires considering the specific spatial interaction between cold pool (CP) gust fronts, namely one where two CPs collide [3–5]. By tracking CPs, we determine their maximal radii  $R_{\max} \sim 20$  km and show that cloud-free regions exceeding such radii always grow indefinitely, whereas smaller ones often decay. Our theory and conceptual modeling describe a mechanism, where cloud-free regions in RCE are likely to form when CPs have small  $R_{\max}$  and cannot replicate, whereas large  $R_{\max}$  hampers such cavities. Our findings imply that the dynamics of self-aggregation are crucially controlled by CP interaction, and known feedback may only be required in stabilizing the final, fully-aggregated state.

## I. INTRODUCTION

When rain evaporation is strong, so is the associated sub-cloud cooling and density increase [6, 7], forcing the resulting cold pools (CPs) to spread quickly and cover larger distances [8–10]. Such strong CP activity has repeatedly been suggested to hamper convective self-aggregation in radiative-convective equilibrium (RCE) numerical experiments [1, 11–13].

In these simulations, the atmosphere gradually organizes from an initial, apparently random, pattern of convective updrafts into an inhomogeneous pattern with one or few strongly convecting patches, but an otherwise nearly precipitation-free domain [1, 2, 14–16]. When rain evaporation is removed, self-aggregation was found to be favored.

Physical processes discussed as contributing to self-aggregation are positive feedback between latent and sensible heat fluxes, radiation, and clouds, as well as their influence on the atmospheric circulation. The early stage of self-aggregation is characterized by the appearance of small dry regions, within which rain is suppressed [17]. Along with this suppression, further drying was reported to occur through radiative cooling and the resulting subsidence, as well as changes in surface fluxes. In the later stage, dry patches expand and merge, eventually leaving only one contiguous moist region. A remarkable aspect of self-aggregation is hysteresis, by which it refuses to disaggregate, once formed, even when initially-required feedback is removed [12, 18, 19].

CPs are capable of mediating organization, as they effectively relay “information” between one precipitating

cloud and its surroundings. Physically, CPs spread as density currents along the surface, carry kinetic energy and can modify the thermodynamic structure of the environment near their edges [3, 4, 20]. CPs can then act to pattern the convectively unstable atmosphere, as the loci where new convective cells emerge, are not independent of the loci at which the previous cells dissipate. In particular, new cells were suggested to be spawned by the CP gust front alone, or by collisions between mobile gust fronts [4, 21, 22], and several conceptual studies, formulating CPs as cellular automata, have resulted from the notion of CP interactions [5, 23, 24].

We analyze large eddy simulations, which sufficiently resolve CP gust fronts, their spreading and interaction (Fig. 1A, and *Materials and Methods*). By employing a CP tracking method, where particles are placed at the edge of active precipitation cells and advected with the horizontal flow surrounding these precipitation cells, we are able to track the evolution of these CPs. Indeed, CPs predictably form shortly after rain falls through the boundary layer, and initially spread horizontally at speeds of approximately  $3 \text{ m s}^{-1}$ . However, due to frictional forces and mixing, CPs do not grow indefinitely — in our simulations, they typically do not exceed radii of  $R_{\max} \approx 20$  km, a value commensurate with previous simulations [8] and observations [25–27].

When examining our simulations, new precipitation cells often emerge in close proximity to the interfaces between the gust fronts from two distinct CPs. These gust fronts have usually become immobile by the time a new precipitation event emerges, but tend to generate positive water vapour anomalies both near the surface and aloft. The time delay can be as large as 3–5 hours, which we quantify by identifying the time until CPs reach their maximal radius and the total budget on CPs in steady state. Despite this delay, the location of newly emerging

\* silas@nbi.ku.dk

† haerter@nbi.ku.dk

cells is systematically positioned near the collision lines formed by previous CP gust fronts, a non-random organizational pattern should hence be expected.

## II. RESULTS

We first characterize the patterning observed in the spatial distribution of precipitation cells in a 30-day simulation of convective self-aggregation. We discuss the formation and dynamics of dry patches and the appearance of marked, non-random, line-segments, which connect precipitation cell centers and are often nearly perfectly straight. To explain both features, we then bring forward a simple model, based on the interaction of expanding circles, which captures the interaction between CP gust fronts and their spawning of subsequent precipitation events.

### A. Cavities need a critical size to either grow or die

Using a tracer method, we track CP gust fronts in RCE (Fig. 1A) (*Details: Methods, Tracking of cold pools*). The tracking allows us to study the life cycle of CPs after they are initiated by a given precipitation event. Similar to results reported elsewhere [27, 28], CP gust fronts initially advance rapidly, but monotonically decrease their radial velocities (Fig. 1B). It is found that even the largest CPs observed typically do not exceed radii of 20 km in the model setup used here.

We now also track the cavities emerging in long RCE simulations (*Details: Methods, Tracking of cavities*). An initial population of relatively small cavities is already present two days after the onset of precipitation. When following the growth of these cavities, some reach larger sizes and eventually contain points that exceed a critical distance  $d_0 > R_{\max}$  from any precipitation cell (red patches in Fig. 1C–D and Fig. S2). We identify a characteristic value of  $R_{\max} \approx 20$  km, for which it is found that essentially all cavities containing points with  $d_0 > R_{\max}$  grow indefinitely, that is, their areas increases without bound (Fig. 1E). Cavities for which all points lie below this threshold may decay in area. Unbounded growth of some cavities causes merging events to take place, whereby multiple cavities connect to form even larger ones. Furthermore, by analyzing the growth rate of all cavities, we find that small cavities ( $R_{\max} < 20$  km) have a tendency to shrink while bigger cavities have a tendency to grow (Fig. 1F).

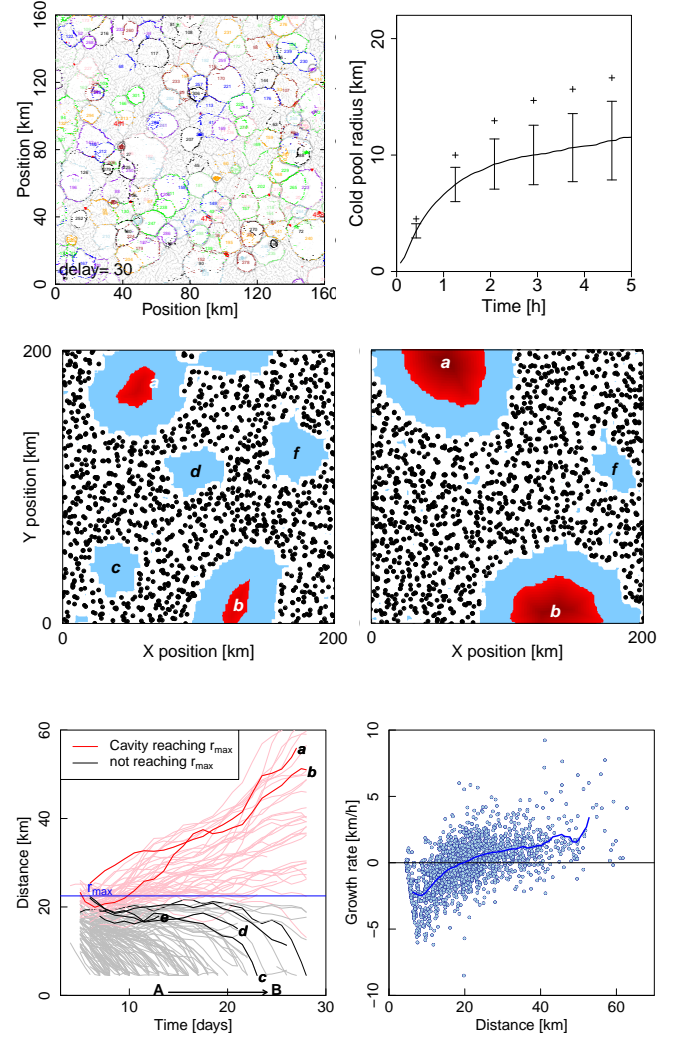


FIG. 1. **Cavities need a critical size to either grow or die.** (A) Tracking the cold pools (CPs) is done by assigning  $N$  tracers to each rain event and let the tracers move radially out by the wind field (see *Tracking of cold pools*). (B) The CPs grow fast the first hour after initialization thereafter their growth saturates. The crosses show 90% extremes. (C–D) Five cavities (blue patches labeled  $a$ – $e$ ) identified in LES data where black dots are the CP centers. Red patches are areas where the distance to a CP center is larger than 20 km. (C) CP centers on day 14 and (D) day 24. Between these two time windows, cavities with white labels ( $a$ – $b$ ) grow while black labels ( $c$ – $e$ ) shrink. (E) The size evolution of all cavities identified in this data set. Black cavities do not reach the critical size,  $R_{\max}$ , while red cavities do. The five cavities in panel C–D are highlighted with lowercase letters while the timing of panel C–D is highlighted with capitals. (F) The growth rate of all cavities as a function of size (light blue dots). The black line shows steady-state, and the blue line shows the average for a given size.

## B. Transient line segments emerge in LES data

We connect all CPs that have the potential to interact with each other by the *line-of-sight* (dotted grey lines in Fig. 2A–B). Two CPs are within the line-of-sight of one-another if no other CP center is inside the circle with the centers of the two CPs in question on its rim (Fig. S1). We show analytically, that in a random seeding each CP center will on average have four neighbors within the line-of-sight (*Details*: SI), and confirm this by numerical simulations (Fig. 2C). Throughout the simulations, LES data show a significantly lower average connectivity due to a higher fraction of CPs with only two or three line-of-sight neighbours (see Fig. 2C inset). This points towards the appearance of lines in LES data.

When inspecting Fig. 1C–D, it is qualitatively apparent that some cells form line-like structures. To quantify, if such linear structures appear more frequently than would be expected at random, we introduce the *line index*. The line index is defined based on local groups of CPs (solid black lines in Fig. 2A–B). For a CP center to be involved in a line, it and its neighbors must have exactly two neighbors inside the group (green points in Fig. 2A–B).

We then quantify the line index as the RCE simulations develop and compare that to a randomized control (Fig. 2D). At all times, we find a significantly higher fraction of lines than expected from a randomized sample. At the intermediate stage (day 3–8), the line index drops due to temporal clustering in the LES data. Our high time resolution data set shows a line index that is twice as large as its random counterpart, and the lines are even visible to the bare eye (SI: Movie 1). Our first data set, LES (I), is more coarse-grained and therefore has higher connectivity and a lower line index (Fig. 2C–D). We further note by watching Movie 1 that the lines tend to grow and decay in one direction only.

By noting the green dots in Fig. 2A that are outside the close-up area (Fig. 2B), it is clear that most lines must be very short and only a few are as long as the one shown in Fig. 2B. This is confirmed in Fig. 2E where we instead of using the line index determine the maximum length of all tracks at two specific days (see *Tracking of cold pools*). We fit the length to  $P^x$  and show  $P = 0.4$  in Fig. 2E. This result we get back to in the next section. In the same figure, we show that the presence of long lines does not change much with time.

Already from Fig. 2C–D, it is clear that the spatial pattern of convective cells is non-random immediately after the simulation start. To confirm this, we measure the shortest distance from one track ID to the nearest neighbor with a different track ID and do the same for a random seeding. We find that the majority of CPs are further apart than what would be expected from random (Fig. 2F). We attribute this positioning to a repulsive effect, caused by the buoyancy decrease from rain-evaporation. From Fig. 2F, we estimate  $R_{\min} \approx 10$  km, and find it to be unchanged with time.

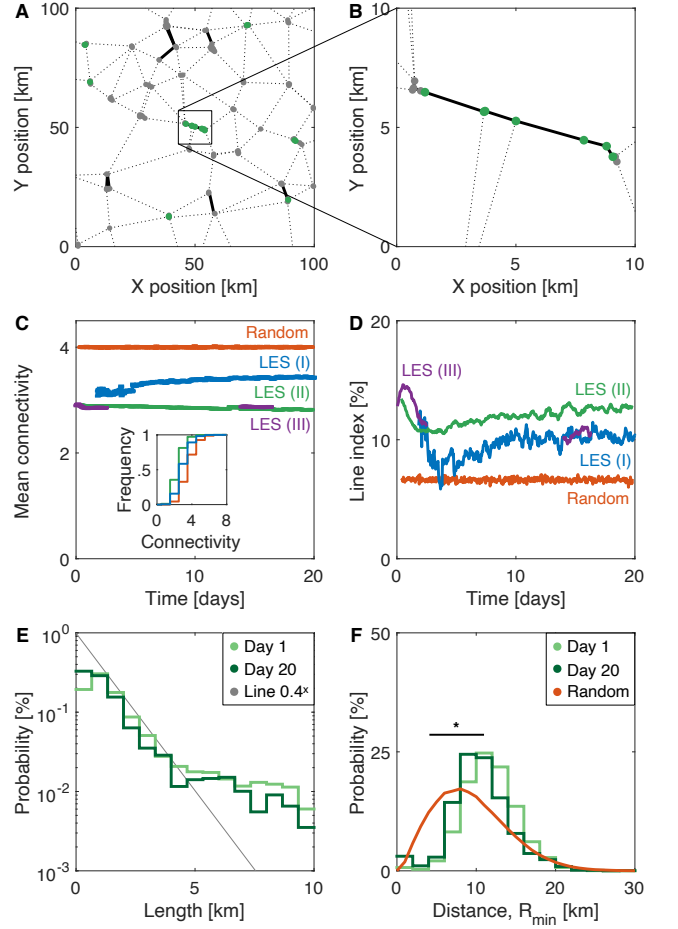


**FIG. 2. Transient line segments emerge in LES data.** (A) A subset of LES (II) cold pool (CP) centers at day 10 illustrating the line-of-sight and the line index. Two points are within the line-of-sight if no other points are closer to the midpoint between the two points in question (grey dashed lines). Of these links only those that are shorter than the typical length  $l = \sqrt{1/N}$  constitute a group (black solid lines). Within each group, only those nodes with them and their neighbors having connectivity two represent a line segment (green nodes). The line index is the fraction of nodes obeying these rules. (B) Close-up of the line in (A). (C) The average line-of-sight connectivity is significantly lower in the LES data (blue, green, and purple) compared to a randomized control (red). The standard error of the mean (SEM) is smaller than the thickness of the lines. The inset shows the accumulated frequency of the number of connections in LES (I) (blue) and (II) (green) relative to the control (red) on day 10. (D) The line index of LES data (blue, green, and purple) is higher than the control which has a line index of  $6.6 \pm 0.3$  (red). (E) The distribution of line lengths at early and late times of LES (II). The grey line is  $0.4^x$ . (F) The separation distance between different CP centers (green) in LES (II) is higher than the theoretical distribution for random positioning (red) and unchanged with time (light vs. dark green). Two-sample Kolmogorov-Smirnov tests showed  $p < 0.001$  statistical significance (marked by \*). A sliding time window of 24 hours is applied in (C–D) and of 6 hours in all other panels. The results are insensitive to the length of the sliding time window. All LES (I) and (II) CP centers are shown in Movie 1.

### C. Circle model captures cavity and line formation

We now introduce a model consisting of growing and colliding circles representing CPs. While we earlier [5] only looked at the dynamics of 3-CP interactions, we now modify the model to focus only on 2-CP interactions. In short, the model is initialized with  $N$  points randomly located on a 2D domain of size  $1000 \text{ km} \times 1000 \text{ km}$  with double periodic boundary conditions (to mimic an infinite domain). All points grow into circles (two highlighted in Fig. 3A) with equal and constant radial speed ( $v_r \equiv 5 \text{ km/h}$ ). When two circle rims (the gust fronts) collide, they instantaneously create a new point (bold black dot in Fig. 3A–B) that then starts growing, again at speed  $v_r$ . This process continuous until the system dies out, i.e., no more circles can be produced (for details see *Mathematical model*). Initially, in each 2-CP collision, we only consider the first, unique, collision point between two circles, but later we relax this constrain.

The simplest 2-CP model includes a minimum radius,  $R_{\min}$ , that the circles need to reach, in order to be able to replicate. Physically, CPs that are smaller than  $R_{\min}$  are too cold, hence negatively buoyant, to initialize new CPs. Mathematically,  $R_{\min}$  conveniently avoids singularities, i.e., infinitely rapid replication, that otherwise would unfold when three circles are located in a triangular geometry where all subsequent generations induce three new circles that are located in a progressively smaller area (inset in Fig. 3B). In Fig. 3C, we present a snapshot of a simulation. We note the presence of cavities and the visual similarity with LES results in Fig. 1C–D. In Fig. 3D, we explore the separation distance between circle centers and compare that to Fig. 2F. We find a fixed  $R_{\min} = 8 \text{ km}$  to give comparable results to LES. We note that  $R_{\min}$  varies more in LES compared to the model.

We now add a maximum radius,  $R_{\max}$ , beyond which the circles become passive and cannot replicate. This parameter mimics the decrease in energy and momentum as CPs grow, mix with environmental air, and lose momentum through surface drag. For simplicity,  $R_{\min}$  and  $R_{\max}$  are fixed for all circles throughout a simulation. Fig. 3E shows how lowering  $R_{\max}$  results in shortening the duration of the model simulation — leading to faster cavity formation and therefore self-aggregation.  $R_{\max} = \infty$  continues for a very long time. For small  $R_{\max}$ , this model predicts a final collapse of the system — a feature that LES-simulated self-aggregation would not develop (see also model dynamics in Movie 2).

Finally, we want to capture the formation of lines shown in Fig. 2. For this, we return to the grey lines in Fig. 2E and Fig. 3B. We suggest that a band of CPs can be formed along the collision curve between two CPs. In the model, we separate these new circles by a fixed distance  $\delta \equiv 1 \text{ km}$ , and let subsequent circles emerge along the curve with a probability  $P = 0.4$ . We find that this gives a line index that drops due to the overall decay of the model (Fig. 3F). However, initially the line index is comparable to the line index found in LES (Fig. 2D).

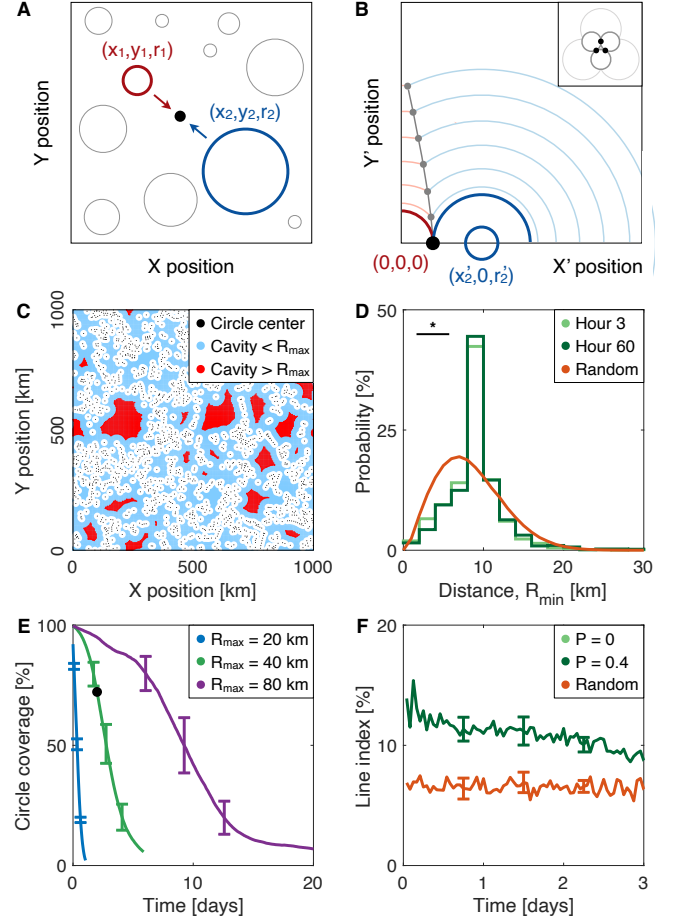


**FIG. 3. Circle model captures cavity and line formation.** (A) At a general time in the model, cold pools (CPs) are represented by circles of different sizes. Two circles (blue and red) will collide at the midpoint between their circles' rim if the midpoint (black dot) is not blocked by other circles. (B) To find the collision point analytically, we translate the system in such a way that the smallest circle (red) is moved to origo and reduced to zero radii and the largest circle (blue) is rotated to the  $X'$ -axis. Potential subsequent collision points (grey dots) are separated by a distance  $\delta$  (for details see *Mathematical model*). The inset shows a singularity. (C) Snapshot of a simulation with  $R_{\max} = 40 \text{ km}$  at day 2. The black dots are the circle centers, the white space is the area the circles enclose, the blue space is a distance less than  $R_{\max}$  away from a circle center, and the red space is further away (compare to Fig. 1C–D). (D) The separation distance between circle centers does not change with time in the model (light vs. dark green) and it is statistical different from a randomized control (two-sample Kolmogorov-Smirnov tests showed  $p < 0.001$  marked by \*, compare to Fig. 2F). (E) The fraction of the domain that the circles cover decays with simulation time. The smaller  $R_{\max}$ , the faster it decays. The error bars show the standard deviation for five simulation runs. The black dot shows where panel (C) is taken. (F) The line index (as defined in the caption to Fig. 2A) for  $P = 0$  (light green),  $P = 0.4$  (dark green), and a control (red) (compare to Fig. 2D). All with  $R_{\max} = 40 \text{ km}$ . Throughout the figure,  $N = 3000$ ,  $R_{\min} = 8 \text{ km}$ , and a sliding time window of 3 hours is used. A set of simulations are shown in Movie 2.

### III. DISCUSSION

Typical explanations for convective self-aggregation invoke circulation feedback, by which the interplay between a subsiding and a convecting region stabilizes a persistent rainy patch. The current results however describe the path towards this final state, and show that the interaction of cold pools (CPs) can explain the initial formation of cavities and their eventual growth into ever larger cloud-free subregions. Indeed, CP collision was recently shown to lead to cloud organization [5].

The final aggregated state has repeatedly shown to be associated with an intensely convecting sub-region and a gently subsiding cloud-free environment. Stabilization of this final state is likely accomplished by a circulation feedback, whereby divergence from the subsidence area feeds the emergent "super cold pool" characterizing the convective sub-domain [29]. We argue here, that such circulation feedback are not required for the development of initial cavities and their growth.

We back up our analysis using a simple conceptual model based on expanding circles and their interaction. The choice of two parameters, a minimal and a maximal circle radius, are well-supported by the physics of CPs. We back up  $R_{\min}$  by negative buoyancy anomalies before reaching the lower radius bound, and  $R_{\max}$  by the dissipation of CP momentum when reaching this upper bound. Varying the movement of the gust fronts of the circles in the model is analytically difficult. Although in reality, CPs grow the fastest the first hour, and their growth saturates after a couple of hours (Fig. 1B). Introducing this would require a circle and possibly a time dependent speed factor in Equation 1 and 2. To solve this, we direct the reader to the numerical approach in [5]. On the other hand, a number of improvements can be implemented to make the model more realistic; varying the time point at which the initial circles start growing, introducing a circle specific  $R_{\min}$  and  $R_{\max}$ , introducing noise on the location of new circles, and a time delay between circle collisions and the emergence of a new circle. Sustained activity may be obtained by either adding noise, 3-CP collisions, or circles that spontaneously emerge. However, impressed by the presented model, and to keep the model simple to convey and interpret, we decided not to implement these. In conclusion, we believe, we presented a new quantitative tool that through CP collisions may explain the underlying mechanism for convective self-aggregation.

### IV. MATERIALS AND METHODS

Here, we describe technical details of the large eddy simulation (LES) setup, the tracking of cold pools (CPs) gust fronts, the tracking of cavities, as well as the definition of the mathematical model.

#### A. Simulation data

Several simulations are analyzed in this paper. The largest simulation (I) was carried out by C. Hohenegger, who kindly supplied us with several output variables of this simulation. Large-eddy simulations of this type consume a large amount of computing resources, and we, therefore, refrained from re-simulate these data. Further, not all model outputs can realistically be stored and be made available. To remedy this shortcoming, we carried out a number of additional simulations of only slightly modified setup, to test the sensitivity against modeling choices and to obtain further output variables at high temporal resolution.

(I) We use the 30-day output from the University of California Large Eddy Simulator (UCLA-LES) [30], mimicking the tropical atmosphere over a spatially homogeneous sea surface in radiative-convective equilibrium. To this end, surface relative humidity is set to unity, the surface temperature is set to 301 K. The simulation uses a horizontal grid resolution of 500 m and 63 vertical model level with grid spacing stretching from 100 m near the surface to 400 m near the model top. The horizontal domain size is set to 1024 km x 1024 km. Interactive radiation is simulated according to the Delta-four stream [31], and the simulation employs a two-moment cloud microphysics scheme [32]. Insolation is set to a constant  $650 \text{ Wm}^{-2}$ , similar to [16], where a constant zenith angle of 50 degrees is assumed. Model output is set to 1 h, hence, one three-dimensional field of  $u$ ,  $v$ , and  $w$  wind, as well as rain droplet concentration, is available at this time interval. Surface latent and sensible heat fluxes are computed according to Monin-Obukhov theory.

(II) As a variation to (I), we employ another simulation with a similar setup, but a coarser horizontal model resolution of 2 km and 960 km x 960 km domain size. This simulation is initialized with a less stable initial temperature and moisture profile, leading to substantially more convective activity during the initial phase of the simulation. Yet, after approximately seven simulation days, self-aggregation sets in and cavities grow as before. The simulation is continued until 20 model days have been simulated. The somewhat smaller domain size and simulation duration allow us to output a range of variables at 10 min temporal resolution — enabling tracking of the associated CP gust fronts.

(III) A sensitivity study is carried out, where (II) is repeated, however reducing the surface latent heat fluxes to 70 percent of their potential value. This simulation does not show self-aggregation, even after 20 days of model time.

#### B. Tracking of cold pools

Cold pool (CP) gust fronts are tracked similarly to the tracer particle method discussed in the recent literature [5]. In short, in any given time step particles are placed at

the edges of existing precipitation cells. These particles are then advected along with the horizontal velocity field in the lowest model level ( $z = 50$  m) and settle in the gust fronts surrounding each CP.

### C. Tracking of cavities

Cavities are tracked by first setting a time window  $\Delta T_0$ , over which the pattern of precipitation cell centers is to be observed. A reasonable choice turns out to be  $\Delta T_0 = 24$  hours, as smaller values lead to too much noise along the edges of dry patches, while larger values do not properly warrant the dynamics of dry patches, i.e. growth, decay and merging or splitting events. Our conclusions do not depend on the precise value of  $\Delta T_0$ . For all precipitation cells falling into this time window, we identify the corresponding cell centers by the use of the iterative rain cell tracking method [33], yielding a collection of points  $\bar{c}_i$  in space, where each point  $\bar{c}_i \equiv (x_i, y_i)$  is a point in the two-dimensional plane. We then scan the two-dimensional plane on the original LES grid of  $2048 \times 2048$  points. For each point  $\bar{c}$  on this grid, we evaluate the distances  $d_i(\bar{c}) \equiv |\bar{c} - \bar{c}_i|$  to each cell center  $\bar{c}_i$ . The distance  $d(\bar{c}) \equiv \min \{d_i(\bar{c})\}$  is then defined as the nearest distance of  $\bar{c}$  to any of the centers  $\bar{c}_i$ .

We now define the threshold distance  $d_0 \equiv 3.5$  km. A cavity is defined as a contiguous region of points  $\bar{c}$  with  $d(\bar{c}) > d_0$ , that is, regions composed of points that are all located at distances larger than the threshold  $d_0$  from existing precipitation cells.  $d_0$  is chosen as the approximate upper limit of distance fluctuations in the aggregated sub-region of the domain. Doubling or halving this value would not have any implications for the conclusions drawn from the current study.

### D. Mathematical model

$N$  points are initialized at random locations selected uniformly on a 2D domain of size  $1000 \text{ km} \times 1000 \text{ km}$ . The domain has cyclic boundary conditions in both  $x$  and  $y$  directions. The  $N$  initial points are referred to as generation one. All points grow into circles with equal and constant radial speed ( $v_r \equiv 5 \text{ km/h}$ ), hence spread isotropically in all horizontal directions. The growing circles have centers at  $\bar{c}_i = [x_i, y_i]$  and increasing radii  $r_i$ . At the collision point,  $[x, y]$ , between two circles of generation  $g$  a new circle belonging to the subsequent generation  $g + 1$  emerges instantaneously. This collision point is determined by solving

$$(x - x_i)^2 + (y - y_i)^2 = (r_i + dr)^2, \quad (1)$$

and

$$(x - x_j)^2 + (y - y_j)^2 = (r_j + dr)^2, \quad (2)$$

where  $dr$  is the distance from the two circles' rim to the collision point. In the default model, only collisions that

fall on the straight line between the two circle centers are allowed since that is the collision point with the highest momentum (bold black dot in Fig. 3A–B). We note, this point can be found by the linear constraint

$$y = \frac{x - x_i}{x_j - x_i}(y_j - y_i) + y_i. \quad (3)$$

since this gives a set of three equations (Eq. 1–3) with three unknowns ( $x, y, dr$ ), which generally has two solutions. One solution can be neglected because only positive real solutions are relevant for this model.

However, since we want the possibility to capture subsequent collisions, we stick to a more advanced approach: We translate the system to a new coordinate system where the smaller of the two circles is moved to origo and reduced to zero radius and the other circle is rotated onto the  $x'$ -axis (Fig. 3B). This gives two equations

$$(x')^2 + (y')^2 = (dr')^2, \quad (4)$$

and

$$(x' - x'_j)^2 + (y')^2 = (r'_j + dr')^2, \quad (5)$$

with three unknowns ( $x', y', dr'$ ). If the location of the first collision point (where  $y' = 0$ ) is not already occupied (blocked) by another circle from the same generation, then we initialize it. Theoretically, all subsequent collisions appear symmetrically in two directions away from the first collision point. However, to capture the unidirectional growth of the lines (noted in Movie 1), we only allow subsequent collision points in one direction which we select randomly (as shown in Fig. 3B). These collision points are separated by a distance  $\delta \equiv 1$  km on the  $y'$ -axis, and they emerge with a probability  $P$  under the condition that the previous collision point from the same pair of parent circles was initialized and that the location is not overtaken. We require the first collision point seeded to allow for subsequent collisions. With  $R_{\min} > \delta$  that also implies that subsequent collisions points cannot interact with each other. Seeding all collision points ( $P = 1$ ) in both directions with a small  $\delta$  will result in a Voronoi diagram of circles [34].

Similar to the analytical approach in [5], we do not run the model strictly chronologically. To reduce simulation time, we take advantage of the fact that circles belonging to different generations cannot interact since they grow with equal and constant speed. Hereby, we calculate all collision points for each generation before proceeding to the next generation. Generally, the last circle in any generation will initiate later than the first circle in the next generation. Therefore, when proceeding to the next generation, we go back in time, to the time where the first circle of the current generation was seeded.

We reduce simulation time further by not considering all possible collisions which would be a list of  $N \times (N - 1)$  collisions every generation or roughly  $10^7$  possible collisions for  $N = 3000$ . We limit this list drastically by

only considering circle centers that are within a distance  $2R_{\max}$  from each other. However, in order to run  $R_{\max} = \infty$ , we further limit the list by discarding circle centers whose midpoint is blocked by more than  $\gamma = 30$  circles. We checked that  $\gamma = 30$  is sufficiently high since increasing  $\gamma$  gives identical results with longer simulation time while decreasing  $\gamma$  did not capture all collisions.

The list of potential collision points is calculated for each generation and sorted incrementally by  $dr$ . The system is updated by inserting circles at the collision points in the order they appear. Circles are only initialized if both parent circles are bigger than  $R_{\min}$  and smaller than  $R_{\max}$ , and if the collision point is not occupied by the subsequent generation. This process is repeated for every generation until no more collisions occur.

The mathematical model is implemented in MATLAB and the original source code is available online at <https://github.com/SilasBoyeNissen/Self-aggregation-determined-by-cold-pool-collisions>.

## ACKNOWLEDGMENTS

We thank Steven J. Böing for useful comments and Cathy Hohenegger for providing her RCE simula-

tion results. SBN acknowledges funding through the Danish National Research Foundation (grant number: DNR116). JOH gratefully acknowledges funding by a grant from the VILLUM Foundation (grant number: 13168) and the European Research Council (ERC) under the European Union's Horizon 2020 research and innovation program (grant number: 771859). We acknowledge the Danish Climate Computing Center (DC3).

## AUTHOR CONTRIBUTIONS

J.O.H. ran and processed the large eddy simulations (LES), analyzed the cavities in the LES data, and wrote and revised the manuscript. S.B.N. analyzed the lines in the LES data, developed, implemented and analyzed the circle model, and wrote and revised the manuscript.

## COMPETING INTERESTS

The authors declare no competing interests.

- 
- [1] Cathy Hohenegger and Bjorn Stevens. Coupled radiative convective equilibrium simulations with explicit and parameterized convection. *Journal of Advances in Modeling Earth Systems*, 8(3):1468–1482, 2016.
  - [2] Allison A Wing, Kerry Emanuel, Christopher E Holloway, and Caroline Muller. Convective self-aggregation in numerical simulations: a review. *Surveys in Geophysics*, 38(6):1173–1197, 2017.
  - [3] Adrian M Tompkins. Organization of tropical convection in low vertical wind shears: The role of cold pools. *Journal of the Atmospheric Sciences*, 58(13):1650–1672, 2001.
  - [4] Simon P de Szoëke, Eric D Skillingstad, Paquita Zuidema, and Arunchandra S Chandra. Cold pools and their influence on the tropical marine boundary layer. *Journal of the Atmospheric Sciences*, 74(4):1149–1168, 2017.
  - [5] Jan O Haerter, Steven J Böing, Olga Henneberg, and Silas Boye Nissen. Circling in on convective organization. *Geophysical Research Letters*, 46(12):7024–7034, 2019.
  - [6] Joanne Simpson. Downdrafts as linkages in dynamic cumulus seeding effects. *Journal of Applied Meteorology*, 19(4):477–487, 1980.
  - [7] Nicholas A Engerer, David J Stensrud, and Michael C Coniglio. Surface characteristics of observed cold pools. *Monthly Weather Review*, 136(12):4839–4849, 2008.
  - [8] David M Romps and Nadir Jeevanjee. On the sizes and lifetimes of cold pools. *Quarterly Journal of the Royal Meteorological Society*, 142(696):1517–1527, 2016.
  - [9] Giuseppe Torri, Zhiming Kuang, and Yang Tian. Mechanisms for convection triggering by cold pools. *Geophysical Research Letters*, 42(6):1943–1950, 2015.
  - [10] Paquita Zuidema, Giuseppe Torri, Caroline Muller, and Arunchandra Chandra. A survey of precipitation-induced atmospheric cold pools over oceans and their interactions with the larger-scale environment. *Surveys in Geophysics*, pages 1–23, 2017.
  - [11] Nadir Jeevanjee and David M Romps. Convective self-aggregation, cold pools, and domain size. *Geophysical Research Letters*, 40(5):994–998, 2013.
  - [12] Caroline Muller and Sandrine Bony. What favors convective aggregation and why? *Geophysical Research Letters*, 42(13):5626–5634, 2015.
  - [13] Chris E Holloway and Steven J Woolnough. The sensitivity of convective aggregation to diabatic processes in idealized radiative-convective equilibrium simulations. *Journal of Advances in Modeling Earth Systems*, 8(1):166–195, 2016.
  - [14] Isaac M Held, Richard S Hemler, and V Ramaswamy. Radiative-convective equilibrium with explicit two-dimensional moist convection. *Journal of the atmospheric sciences*, 50(23):3909–3927, 1993.
  - [15] Adrian M Tompkins and George C Craig. Radiative-convective equilibrium in a three-dimensional cloud-ensemble model. *Quarterly Journal of the Royal Meteorological Society*, 124(550):2073–2097, 1998.
  - [16] Christopher S Bretherton, Peter N Blossey, and Marat Khairoutdinov. An energy-balance analysis of deep convective self-aggregation above uniform SST. *Journal of the Atmospheric Sciences*, 62(12):4273–4292, 2005.
  - [17] Christopher E Holloway, Allison A Wing, Sandrine Bony, Caroline Muller, Hirohiko Masunaga, Tristan S L'Ecuyer, David D Turner, and Paquita Zuidema. Observing convective aggregation. *Surveys in Geophysics*, 38(6):1199–

- 1236, 2017.
- [18] Marat F Khairoutdinov and Kerry A Emanuel. Aggregated convection and the regulation of tropical climate. In *29th Conference on Hurricanes and Tropical Meteorology, Amer. Meteorol. Soc., Tucson, AZ*, 2010.
  - [19] Caroline J Muller and Isaac M Held. Detailed investigation of the self-aggregation of convection in cloud-resolving simulations. *Journal of the Atmospheric Sciences*, 69(8):2551–2565, 2012.
  - [20] Wolfgang Langhans and David M Romps. The origin of water vapor rings in tropical oceanic cold pools. *Geophysical Research Letters*, 42(18):7825–7834, 2015.
  - [21] Franziska Glassmeier and Graham Feingold. Network approach to patterns in stratocumulus clouds. *Proceedings of the National Academy of Sciences*, 114(40):10578–10583, 2017.
  - [22] Carlo Cafaro and Gabriel G Rooney. Characteristics of colliding density currents: A numerical and theoretical study. *Quarterly Journal of the Royal Meteorological Society*, 144(715):1761–1771, 2018.
  - [23] Jean-Yves Grandpeix and Jean-Philippe Lafore. A density current parameterization coupled with Emanuel’s convection scheme. Part I: The models. *Journal of the Atmospheric Sciences*, 67(4):881–897, 2010.
  - [24] Steven J Böing. An object-based model for convective cold pool dynamics. *Mathematics of Climate and Weather Forecasting*, 2(1), 2016.
  - [25] Peter G Black. Mesoscale cloud patterns revealed by apollo-soyuz photographs. *Bulletin of the American Meteorological Society*, 59(11):1409–1419, 1978.
  - [26] Paquita Zuidema, Zhujun Li, Reginald J Hill, Ludovic Bariteau, Bob Rilling, Chris Fairall, W Alan Brewer, Bruce Albrecht, and Jeff Hare. On trade wind cumulus cold pools. *Journal of the Atmospheric Sciences*, 69(1):258–280, 2012.
  - [27] Zhe Feng, Samson Hagos, Angela K Rowe, Casey D Burleyson, Matus N Martini, and Simon P Szoek. Mechanisms of convective cloud organization by cold pools over tropical warm ocean during the amie/dynamo field campaign. *Journal of Advances in Modeling Earth Systems*, 7(2):357–381, 2015.
  - [28] Nadir Jeevanjee and David M Romps. Effective buoyancy, inertial pressure, and the mechanical generation of boundary layer mass flux by cold pools. *Journal of the Atmospheric Sciences*, 72(8):3199–3213, 2015.
  - [29] JM Windmiller and Cathy Hohenegger. Convection on the edge. *Journal of Advances in Modeling Earth Systems*, 2019.
  - [30] Bjorn Stevens, Chin-Hoh Moeng, Andrew S Ackerman, Christopher S Bretherton, Andreas Chlond, Stephan de Roode, James Edwards, Jean-Christophe Golaz, Hongli Jiang, Marat Khairoutdinov, Michael P Kirkpatrick, David C. Lewellen, Adrian Lock, Frank Miller, David E. Stevens, Eoin Whelan, and Ping Zhu. Evaluation of large-eddy simulations via observations of nocturnal marine stratocumulus. *Monthly Weather Review*, 133(6):1443–1462, 2005.
  - [31] Robert Pincus and Bjorn Stevens. Monte Carlo spectral integration: A consistent approximation for radiative transfer in large eddy simulations. *Journal of Advances in Modeling Earth Systems*, 1(2):1–9, 2009.
  - [32] A Seifert and KD Beheng. A two-moment cloud microphysics parameterization for mixed-phase clouds. Part 1: Model description. *Meteorology and Atmospheric Physics*, 92(1-2):45–66, 2006.
  - [33] Christopher Moseley, Peter Berg, and Jan O Haerter. Probing the precipitation life cycle by iterative rain cell tracking. *Journal of Geophysical Research: Atmospheres*, 118(24):13–361, 2013.
  - [34] Deok-Soo Kim, Donguk Kim, and Kokichi Sugihara. Voronoi diagram of a circle set from voronoi diagram of a point set: II. geometry. *Computer Aided Geometric Design*, 18(6):563–585, 2001.

## SUPPLEMENTARY INFORMATION

In the supplement, we analytically find the average number of line-of-sight neighbors in a system with randomly positioned cells (Fig. S1), we include a movie of LES (I) and LES (II) cold pool centers, and we follow the development of the cavities in Fig. 1C–D over a longer time (Fig. S2).

### Line-of-sight collisions for random seeding

Consider a total area  $A = \pi R^2$ , which is randomly seeded with  $N$  points. A line-of-sight connection between any two points  $i$  and  $j$  at distance  $r$  exists, if there are no further points located within the circle of radius  $r/2$  centered at  $(\bar{c}_i + \bar{c}_j)/2$  which contains  $i$  and  $j$  (Fig. S1). One must further consider the probability of finding two points at distance  $r$ . For this purpose, define the density of points as  $\rho \equiv N/A = N/\pi R^2$ . Now consider the infinitesimal area  $a(r)dr$  which is the area enclosed by two circles of radii  $r$  and  $r + dr$ . The number of points contained in this area will be

$$n(r)dr = \rho a(r) \approx \frac{2Nr}{R^2} dr. \quad (\text{S1})$$

For any two points at a given distance  $r$ , we now consider the probability  $p(r)$ , that none of the remaining  $N - 2$  points lies within the circle of radius  $r/2$ :

$$P(r) = P_0^{N-2} = \left(1 - \frac{\pi(r/2)^2}{\pi R^2}\right)^{N-2}, \quad (\text{S2})$$

where

$$P_0 = 1 - \frac{\pi(r/2)^2}{\pi R^2} \quad (\text{S3})$$

is the probability, that any single point is not located inside the area enclosed by a circle of radius  $r/2$ . Now the total number of expected line-of-sight connections for a fixed given point to any of the other points can be

computed:

$$N_{LOS} = \int_0^R dr n(r) P(r) \quad (\text{S4})$$

$$= \int_0^R dr \frac{2Nr}{R^2} \left(1 - \frac{r^2}{4R^2}\right)^{N-2} \quad (\text{S5})$$

$$= \frac{4(1 - (\frac{3}{4})^{N-1})}{1 - N^{-1}}, \quad (\text{S6})$$

which gives  $\lim_{N \rightarrow \infty} N_{LOS} = 4$ . Hence, when repeating for all  $N$  and avoiding double-counting of connections, one obtains that there are  $2N$  line-of-sight connections.

### Movie 1: LES cold pool centers

All cold pool (CP) centers in **(A)** LES (I) and **(B)** LES (II) illustrated with a sliding time window of 6 hours. The first CPs appear 35 hours later in LES (I) compared to LES (II). The spatial domain of LES (I) is slightly bigger than LES (II) (see *Simulation data*). Each color indicates a unique track (see *Tracking of cold pools*). The black box in LES (II) at 240–245 hours shows the subset illustrated in Fig. 2A. Note the formation of cavities and the appearance of lines of length up to  $\sim 10$  km.

### Movie 2: Model circle centers

All circle centers in four different model simulations. **(A)**  $R_{\max} = 20$  km and  $P = 0$ . **(B)**  $R_{\max} = 40$  km and  $P = 0$ . **(C)**  $R_{\max} = 80$  km and  $P = 0$ . **(D)**  $R_{\max} = 40$  km and  $P = 0.4$ . In all four simulations  $N = 3000$ ,  $R_{\min} = 8$  km, the sliding time window is 3 hours, and the initial seedings are identical. The color scheme is similar to Fig. 3E. We note that cavities form the fastest when  $R_{\max}$  is small (panel A). Generally, cavity formation results in model collapse (see also Fig. 3E). Panel B at time 47–49 hours is identical to Fig. 3C. In panel D, we note the formation of short lines.

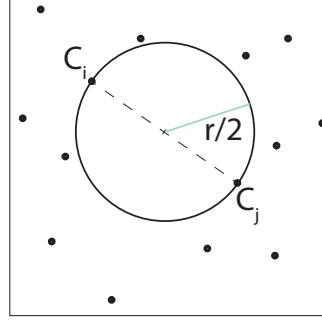


FIG. S1. **Line-of-sight connection.** Schematic illustrating points in a two-dimensional domain and highlighting two particular points  $\bar{c}_i$  and  $\bar{c}_j$  at distance  $r$  that have a line-of-sight connection. The circle of radius  $r/2$  including the two points  $\bar{c}_i$  and  $\bar{c}_j$  highlights the line-of-sight condition, namely, that no other points must be contained within the circle shown.

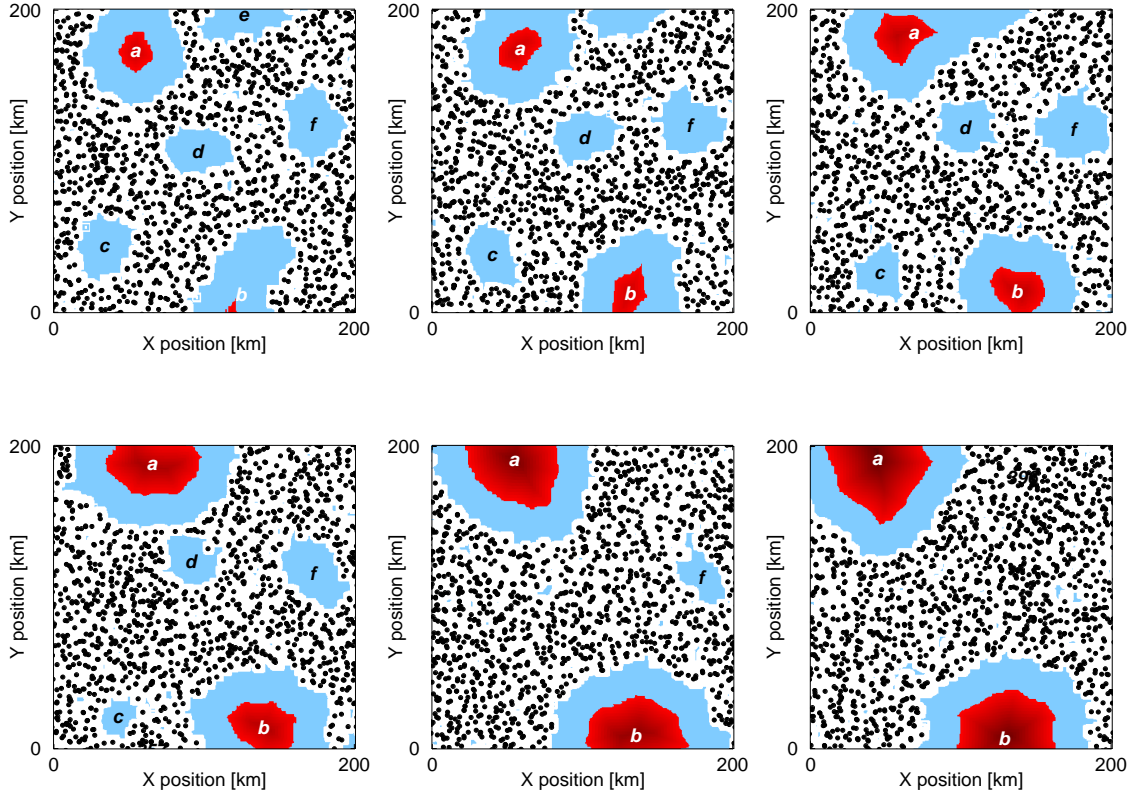


FIG. S2. **Patterns of cells at various times during self-aggregation.**